Check for updates

Fatigue & Fracture of Engineering Materials & Structures

WILEY

FFEMS Fatigue & Fracture of Engineering Materials & Structures

ORIGINAL ARTICLE OPEN ACCESS

Impact Toughness and Fatigue Crack Propagation in Carbide-Free Bainite: The Adverse Role of Retained Austenite and Martensite-Austenite Islands

Oguz Gulbay | Alexander Gramlich | Ulrich Krupp

Steel Institute, RWTH Aachen University, Aachen, Germany

Correspondence: Oguz Gulbay (oguz.guelbay@iehk.rwth-aachen.de)

Received: 28 February 2025 | **Revised:** 24 May 2025 | **Accepted:** 24 June 2025

Funding: The authors received no specific funding for this work.

Keywords: bainite | crack propagation | fracture | MA island | retained austenite | steel

ABSTRACT

The deformation behavior of carbide-bearing bainite (CBB) and carbide-free bainite (CFB) under various loading conditions is investigated. Retained austenite (RA) in CFB enhances strength and ductility only under uniaxial tension through gradual strain-induced martensitic transformation, yet deteriorates impact toughness and fatigue crack resistance. CBB, however, shows superior impact toughness and stronger resistance to crack propagation with effective fatigue crack deflection at prior austenite grain boundaries (PAGB). Martensite-austenite (MA) islands and unstable austenitic constituents induce intergranular fracture in CFB by forming a brittle network along the PAGBs when combined with localized deformation. Furthermore, weakened PAGBs fail to provide an effective barrier against transgranular fracture. In this case, rapid PAG debonding through MA islands leads to cleavage fracture in Charpy tests, whereas ductile fracture occurs in crack propagation tests. These results highlight the need to carefully design CFB microstructures, particularly RA, to achieve optimal mechanical performance for specific applications.

1 | Introduction

Improving the mechanical properties of steel alloys is important for enhancing the longevity and reliability of engineering components. Beyond engineering performance, this also contributes to environmental sustainability by promoting the circularity of the steel industry [1, 2]. Over the decades, different types of bainitic microstructures have drawn considerable research attention due to their promising properties and their low-cost alloying concepts [3, 4]. Modifications in chemical composition and process parameters significantly influence the microstructure of bainitic steels, which, in turn, substantially influence the performance of the steel. It is well known that the addition of ~1 wt% of Si suppresses the carbide precipitation, making the surplus carbon available for enrichment in surrounding austenite [5–7]. In this way, retained austenite is introduced to the microstructure as a secondary phase to form carbide-free bainite (CFB) as opposed to cementite in carbide-bearing bainite (CBB).

In CFB microstructures, RA exists primarily in two morphologies: nanoscale films that form between bainitic ferrite (BF) plates and blocky type that forms preferably on prior austenite grain boundaries (PAGB). Film-like RA is generally more stable due to its size and higher carbon content, which enhances its resistance to transformation under thermal or mechanical stress [5]. On the other hand, blocky RA tends to form in larger sizes with lower carbon contents, making it more susceptible to transformation, leading to martensite-austenite (MA) islands formation during cooling or under mechanical stress [8]. Therefore, they are often considered undesirable because they may negatively influence the mechanical properties.

This is an open access article under the terms of the Creative Commons Attribution License, which permits use, distribution and reproduction in any medium, provided the original work is properly cited.

© 2025 The Author(s). *Fatigue & Fracture of Engineering Materials & Structures* published by John Wiley & Sons Ltd.

Summary

- Performance of carbide-free bainite is contradictory under various loading conditions.
- This discrepancy originates from austenite's response to changed deformation mechanisms.
- Stability, morphology, and distribution of austenite influence fracture behavior greatly.
- The crack/PAG-boundary angle alters the crack path near unstable austenitic constituents.

The primary advantage of RA in CFB is the martensitic transformation due to the transformation-induced plasticity (TRIP) effect under mechanical loading. This mechanism results in exceptional quasistatic tensile properties due to pronounced strain hardening, leading to a well-balanced ultimate tensile strength (UTS) and elongation [9, 10]. Consequently, CFB alloys outperform conventional CBB alloys in quasistatic tensile properties [11, 12] and achieve comparable results to high-strength steels, such as tempered-martensite based steels, without a substantial loss in strength [5]. However, under fatigue loading, the influence of RA is rather complicated. It has been reported that RA can be beneficial by transforming into martensite at the crack tip, thereby absorbing the energy for crack propagation and decelerating the progression of fatigue cracks. Conversely, the existence of unstable blocky RA and MA islands can be detrimental. Gao et al. [13] showed that film-like RA between BF plates arrests the fatigue crack via martensitic transformation, whereas MA island and blocky RA on PAGBs cause intergranular fracture, deteriorating the fatigue properties. Similarly, although the existence of RA can improve the impact toughness through the TRIP effect, it has also been stated that the existence of MA islands and unstable blocky RA can lead to brittle fracture [14–16]. Therefore, the stability, fraction, size, morphology, and location of these microstructural constituents in bainitic applications strongly influence the mechanical performance; thus, the microstructure optimization for the intended application becomes crucial.

Although tensile tests are widely used to assess the performance of bainitic steels, a broader understanding of their mechanical performance requires testing under various loading conditions, especially for complex microstructures like CFB. This study builds upon previous work [12] in which the uniaxial tensile behavior and fatigue limit of the same material conditions were studied. In contrast to earlier investigations, the present work expands the scope by incorporating Charpy impact testing and bending fatigue crack propagation experiments to assess mechanical response at different loading conditions. Moreover, the experimental findings are supported by thorough microstructural and fractographic examinations. By including these additional investigations, a more comprehensive understanding of how retained austenite and MA islands influence the fracture behavior is provided. In this way, it is aimed to establish a broader range of service-relevant conditions by enabling a more detailed understanding of the microstructure-performance relationships in CFB microstructures.

2 | Materials and Methods

Two steel ingots (80 kg each) with nominal compositions of Fe-0.2C-2.5Mn and Fe-0.2C-2.5Mn-1.5Si (wt%) were produced using a laboratory-scale vacuum induction furnace. The $140 \times 140\,\text{mm}^2$ ingots were homogenized at 1200°C and forged down to $60 \times 60\,\text{mm}^2$ billets. Following this, a second homogenization at 1200°C for 5 h was carried out, followed by furnace cooling. The chemical compositions of the alloys, as measured by optical emission spectroscopy (OES), are presented in Table 1, with carbon content determined via combustion analysis. The addition of 1.5 wt% Si to the second alloy was intended to inhibit cementite precipitation during the bainitic transformation. Hence, the first alloy was designed to produce carbide-bearing bainite (CBB), whereas the second alloy was designed to produce carbide-free bainite (CFB). Accordingly, the first alloy was denoted as CBB, whereas the second was denoted as CFB. In order to generate bainitic microstructures, an isothermal heat treatment was conducted in a salt bath at 400°C for 45 min after austenitization for both alloys. The isothermal heat treatments were conducted above the martensite start temperature (M_s), which was determined as 384°C and 374°C for CBB and CFB, respectively. The graphical representation of heat treatment is shown in Figure 1a. Initial investigations on microstructure and mechanical properties have been published in previous works, which were conducted with the same materials and the same chemical compositions [12, 17].

Uniaxial tensile tests were conducted using B5 × 25 cylindrical tensile specimens with a gauge diameter of 5 mm and a gauge length of 25 mm. The tests were performed at room temperature on a ZWICKROELL Z100 universal electromechanical testing machine (ZwickRoell GmbH & Co. KG, Germany) at a strain rate of $10^{-3}\,\text{s}^{-1}$. Three tensile specimens were tested for each condition. Charpy impact tests were carried out on a 300-J instrumented Charpy impact test machine using standard V-notched $10 \times 10 \times 55\,\text{mm}^3$ specimens. For each material state, three tests were performed at room temperature.

Crack propagation tests were performed on a RUMUL CRACKTRONIC (Russenberger Prüfmachinen AG, Switzerland) resonance testing machine at a stress ratio of $R = -1$. For the tests, single-edge notched bend (SENB) specimens were used. The specimen geometry is shown in Figure 1b. Before performing each test, a precrack was introduced into the specimen with a length of

TABLE 1 | Chemical composition of the studied alloys in wt%.

Alloy	C	Mn	Si	Al	P	S	Cr	Mo
CBB	0.18	2.48	0.01	0.002	0.003	0.002	0.04	0.01
CFB	0.19	2.38	1.48	0.003	0.003	0.003	0.04	0.01

14602695, 0, Downloaded from https://onlinelibrary.wiley.com/doi/10.1111/ffe.70025 by Rwth Aachen University Zentraler Rechnungseingang, Wiley Online Library on [29/07/2025]. See the Terms and Conditions (https://onlinelibrary.wiley.com/terms-and-conditions) on Wiley Online Library for rules of use; OA articles are governed by the applicable Creative Commons License

approximately 1.3 mm by cyclic loading with stepwise reduction of the bending moment to ensure a small plastic zone at the crack tip. The threshold value of the stress intensity factor (SIF) range (ΔK_{th}) for technical crack propagation was determined using the load-shedding procedure. Following ISO 12108 [18], the SIF range (ΔK) was gradually reduced until no technically relevant crack growth was observed (multiple data points with a linear regression between $da/dN < 10^{-11}$ m/cycle and $da/dN < 10^{-10}$ m/cycle). Lastly, the stable crack propagation was monitored at a constant bending moment to observe crack propagation behavior in the Paris regime of the log da/dN versus log ΔK curve [18].

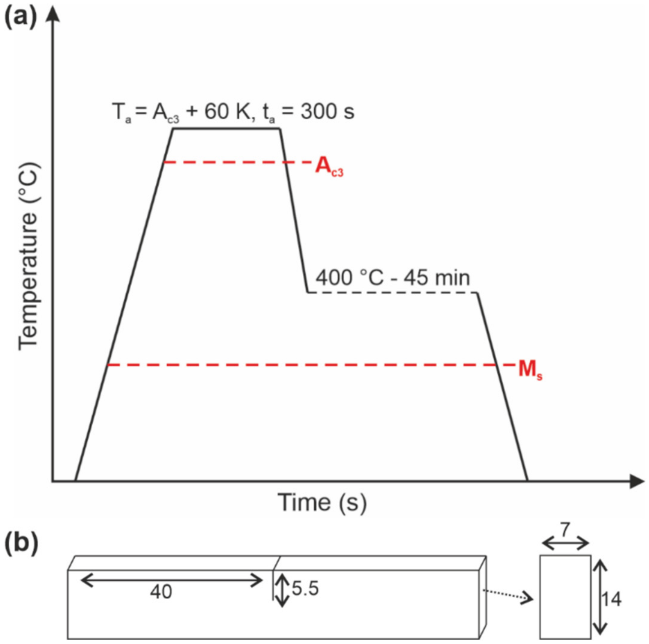

FIGURE 1 | (a) Graphical representation of heat treatment. (b) Specimen geometry of the single edge notch bend (SENB) specimen. Dimensions are given in mm. [Colour figure can be viewed at wileyonlinelibrary.com]

Microstructural and fractographic analyses were conducted using a field-emission gun ZEISS SIGMA SEM (Carl Zeiss Microscopy GmbH, Germany) with a secondary electron (SE) detector. Specimen preparation for microstructural examinations involved mechanical grinding with SiC abrasive paper up to 1200 grit, followed by polishing using diamond paste with particle sizes of 6 and 1 µm, respectively. The polished specimens were then etched with 3% HNO_3 (Nital) to reveal the microstructure. For electron backscatter diffraction (EBSD) analysis, the specimens underwent a final surface polishing with oxide polishing suspension (OPS) for 20 min after the final mechanical polishing step. The EBSD measurements were conducted using a NORDLYS NANO detector (Oxford Instruments, Great Britain) with a 75-µm aperture, an accelerating voltage of 20 kV, a working distance of 17 mm, and a step size of 75 nm. Quantitative X-ray diffraction (XRD) was used to determine the retained austenite (RA) fractions in the CFB alloys. Measurements were performed using a Stresstech Xstress G3 diffractometer with a Cr source, operating at 30 kV and 8 mA.

3 | Results

The achieved SEM images of CBB and CFB alloys after isothermal heat treatment are shown in Figure 2. The microstructure of CBB alloy is composed of bainitic ferrite (BF) as the primary phase and cementite as the secondary phase (cf. Figure 2a). In the case of CFB, it was observed that cementite precipitation was suppressed by Si alloying, as intended. The microstructure mainly consisted of plate-like BF and retained austenite (RA) films between BF plates. RA formation was not only detected between the BF plates but also on prior austenite grain (PAG) boundaries with different morphological features, such as blocky and elongated. Moreover, big blocky martensite-austenite (MA) island formations were detected in

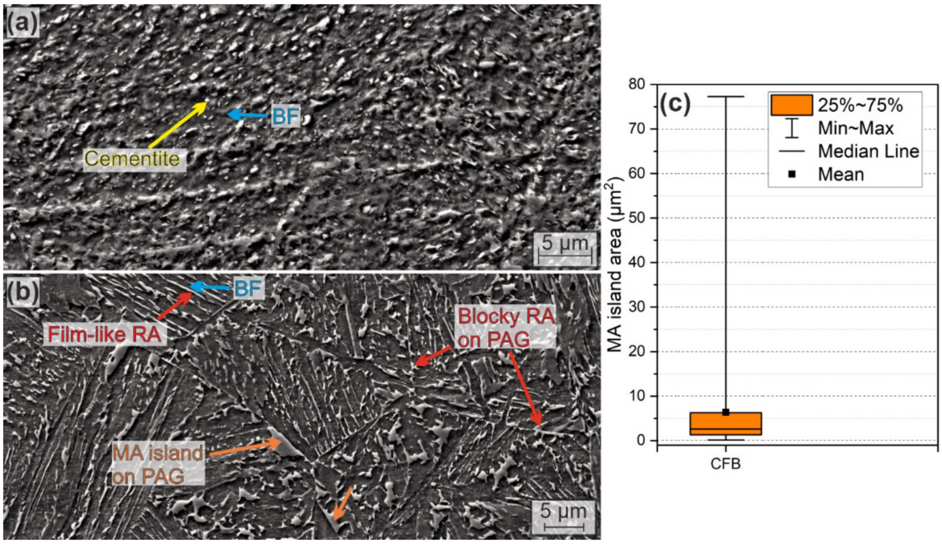

FIGURE 2 | SEM images of (a) CBB and (b) CFB alloys. Images were acquired from an undeformed state. (c) Statistical evaluation of MA islands, showing the minimum and maximum values, mean, median, and interquartile range (25th–75th percentile). [Colour figure can be viewed at wileyonlinelibrary.com]

14602695, 0, Downloaded from https://onlinelibrary.wiley.com/doi/10.1111/ffe.70025 by Rwth Aachen University Zentraler Rechnungseingang, Wiley Online Library on [29/07/2025]. See the Terms and Conditions (https://onlinelibrary.wiley.com/terms-and-conditions) on Wiley Online Library for rules of use; OA articles are governed by the applicable Creative Commons License

addition to RA as a secondary phase (Figure 2b). The statistical evaluation of the MA island size in CFB steel, based on 250 individual measurements, is displayed in Figure 2c. The average MA island area was determined as 6.4 μm^2, whereas minima and maxima exhibited a significant difference between 0.1 and 77.3 μm^2, indicating an inhomogeneous size distribution of MA islands in the microstructure. Furthermore, the area fraction of the MA islands was determined to be 10.3% (cf. Table 2). The majority of the MA islands were located on or near the PAG boundaries, as highlighted in Figure 2b, although some were observed within the PAG interiors. Additionally, it is important to note that the PAG sizes of CBB and CFB were measured to be approximately 54 and 60 μm, respectively, indicating that both alloys exhibit comparable PAG sizes.

Engineering stress–strain curves of the studied alloys are displayed in Figure 3a. Both alloys show continuous yielding behavior and uniform plastic deformation; however, the CFB alloy exhibited superior tensile properties to the CBB alloy, with a relative increase from 738 to 765 and from 866 to 1134 MPa for yield strength (YS) and ultimate tensile strength (UTS), respectively. Uniform elongation (UE) as well as total elongation increased from 4.2% to 11.6% and 13.4% to 19.4% (cf. Table 3). Additionally, EBSD measurements were accomplished before and after tensile testing to examine the RA behavior during deformation. Figure 3b,c displays the band contrast maps superimposed with the RA phase before and after the tensile test, respectively. It is displayed that only a trace amount of RA was detected after deformation, unlike the undeformed state. The RA fractions obtained via XRD supported these findings, exhibiting 6.1% before deformation and 0.5% after deformation (cf. Table 2).

Contrary to the improved ductility during tensile tests, the impact toughness of CFB was significantly lower than that of CBB, with an impact energy of 52.5 and 10.3 J for CBB and CFB, respectively (cf. Table 3). The fracture surfaces reveal that the CBB alloy exhibited a significant amount of ductile fracture features, mainly at the subnotch area and edges of the specimen (cf. Figure 4a,b), where small dimple areas are visible. When the subnotch area was surpassed, the fracture mode changed to transgranular cleavage surrounded by ductile dimpled regions at the edges of the facets (cf. Figure 5a). In alignment, the maximum force of ~15.5 kN was reached gradually (cf. Figure 5c), indicating plastic deformation rather than sudden brittle fracture. In contrast, the fracture surface of CFB was dominated by brittle fracture characteristics with intergranular and cleavage fracture

TABLE 2 | Area fraction and average size of the MA islands and volume fraction of retained austenite before and after tensile deformation (via XRD) in CFB steel.

MA islands (area fraction)	MA islands (average area)	Retained austenite (before deformation)	Retained austenite (after deformation)
10.3%	6.4 μm^2	6.1%	0.5%

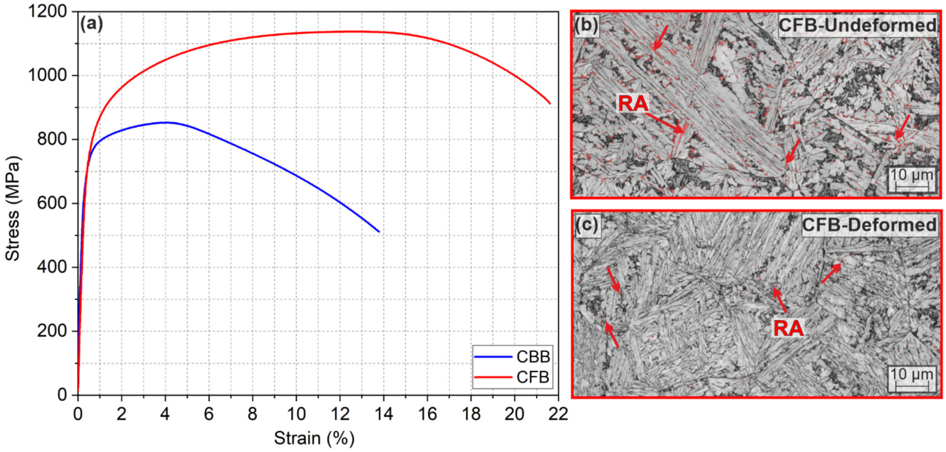

FIGURE 3 | (a) Engineering stress–strain curves of the studied alloys. The EBSD band contrast map, superimposed with the retained austenite phase of CFB alloy (b) before deformation and (c) after deformation. [Colour figure can be viewed at wileyonlinelibrary.com]

TABLE 3 | Quasistatic tensile properties, impact toughness, fatigue limit, ΔK_{th}, m, and C of CBB and CFB alloys.

Material state	YS (MPa)	UTS (MPa)	UE (%)	TE (%)	Impact en. (J)	Fatigue lim. (MPa)	ΔK_{th} (MPa$\sqrt{}$m)	m	C [10^{-12}]
CBB	738∓13	866∓12	4.2∓0.7	13.4∓0.6	52.5∓4.5	343	14.80	2.84	0.24
CFB	765∓5	1134∓4	11.6∓0.6	19.4∓0.2	10.3∓0.5	495	12.55	2.98	0.81

14602695, 0, Downloaded from https://onlinelibrary.wiley.com/doi/10.1111/ffe.70025 by Rwth Aachen University Zentraler Rechnungseingang, Wiley Online Library on [29/07/2025]. See the Terms and Conditions (https://onlinelibrary.wiley.com/terms-and-conditions) on Wiley Online Library for rules of use; OA articles are governed by the applicable Creative Commons License

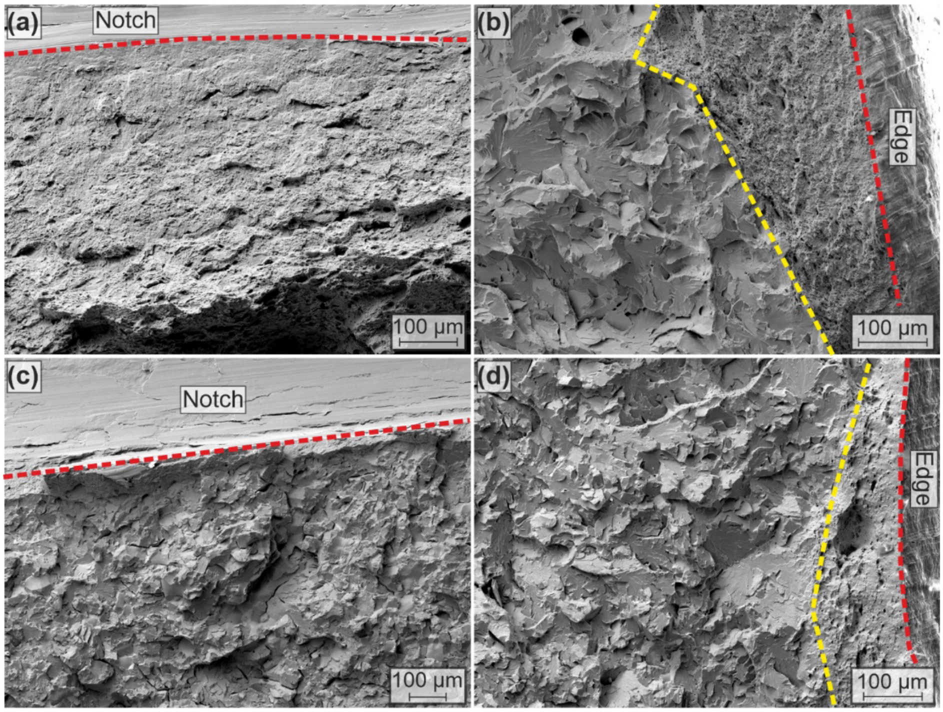

FIGURE 4 | Fracture surface images of (a, b) CBB and (c, d) CFB acquired from Charpy impact test specimens. (a, c) Images taken from the sub-notch area and (b, d) images taken from the edge of the specimens. [Colour figure can be viewed at wileyonlinelibrary.com]

(cf. Figure 4c,d and Figure 5b). Small amounts of ductile fracture dimples at the edges of the specimen were also observed (cf. Figure 4d). The magnified fractography of CFB in Figure 5b shows the grains that were revealed after an intergranular fracture. These results are also reflected in the force-displacement curve of the CFB alloy by brittle failure after the maximum load of 14 kN. Additionally, the integral of the force-displacement curves in Figure 5c shows the clear difference in the values obtained for impact toughness.

The fatigue limit of these alloys has already been determined in a previous study [12] by the staircase testing method using the Dixon and Mood [19] equation. It was revealed that the fatigue limit of CFB is ~150 MPa higher than that of CBB, which is also shown in Table 3. To amend the uniaxial fatigue testing, crack propagation tests were carried out in this study to investigate the crack propagation behavior via resonance bending fatigue experiments. The results of the crack propagation tests are displayed in Figure 6a. Contrary to the fatigue limits, CFB showed a slightly lower threshold SIF range by $\Delta K_{th} = 12.55\,\mathrm{MPa}\sqrt{\mathrm{m}}$, whereas CBB showed $\Delta K_{th} = 14.80\,\mathrm{MPa}\sqrt{\mathrm{m}}$. Moreover, CFB exhibited a faster crack propagation rate in the stable crack growth region. This was reflected in the parameters of the Paris line of CFB as a slightly higher slope m of 2.98 and a higher constant C of 0.81×10^{-12}, whereas the slope m was 2.84, and the constant C was 0.24×10^{-12} in CBB (cf. Table 3). It is worth mentioning that more data scattering occurred during stable crack growth of CFB. Furthermore, the determined fatigue limit and ΔK_{th} values of the studied alloys were used to draw the Kitagawa–Takahashi diagram [20], with El-Haddad modification [21], as presented in Figure 6b. Thereby, the curves represent the region of nonpropagating cracks. Accordingly, the combined results reveal a larger safe zone for CFB alloy, although it has poorer crack propagation characteristics.

The fracture surfaces, acquired from different phases of the crack propagation curve, are shown in Figure 7. As highlighted in Figure 6a, the crack propagation curves are divided into three phases to highlight the fracture surface characteristics in more detail. In the case of CBB, it mostly exhibited ductile fracture characteristics during the whole experiment. In Phases 1 and 2, only ductile fracture behavior with clear fatigue striations was detected, as shown, respectively, in Figure 7a,b. In Phase 3, close to the end of the crack propagation test, some brittle fracture characteristics were formed in addition to ductile behavior, as highlighted in Figure 7c. In this phase, the data scattering was also increased, as shown in Figure 6a. In the case of CFB, the fracture surface exhibited characteristics of brittle and ductile behavior in combination. In Phases 1 and 3, brittle fracture behavior surfaced as a distinct intergranular fracture through the PAGBs (highlighted in Figure 7d,f), whereas ductile fracture characteristics were observed by ductile tearing bainitic blocks containing the morphology of parallel BF plates (cf. Figure 7d,f). In these regions, fatigue striations were also detected, which is a unique feature of ductile fatigue crack propagation behavior. In Phase 2, where the transition occurred before the stable crack propagation region, a plateau formed, as highlighted in Figure 6a. During this phase, only ductile fracture behavior with similar characteristics as the ductile regions in Phases 1 and 2 was monitored (cf. Figure 7e).

In Figure 8, the SEM images and inverse pole figure (IPF) maps of CBB and CFB alloys acquired from the cracked surface perpendicular to the fracture surface are shown. It can be seen that the fatigue crack was effectively deflected by the PAGBs in CBB (cf. Figure 8a). This is also shown in the inverse pole figure (IPF) map of the CBB alloy in Figure 8c more clearly, where the crack was successfully deflected when there was a change in orientation, such as PAG and/or block boundaries.

14602695, 0, Downloaded from https://onlinelibrary.wiley.com/doi/10.1111/ffe.70025 by Rwth Aachen University Zentraler Rechnungseingang, Wiley Online Library on [29/07/2025]. See the Terms and Conditions (https://onlinelibrary.wiley.com/terms-and-conditions) on Wiley Online Library for rules of use; OA articles are governed by the applicable Creative Commons License

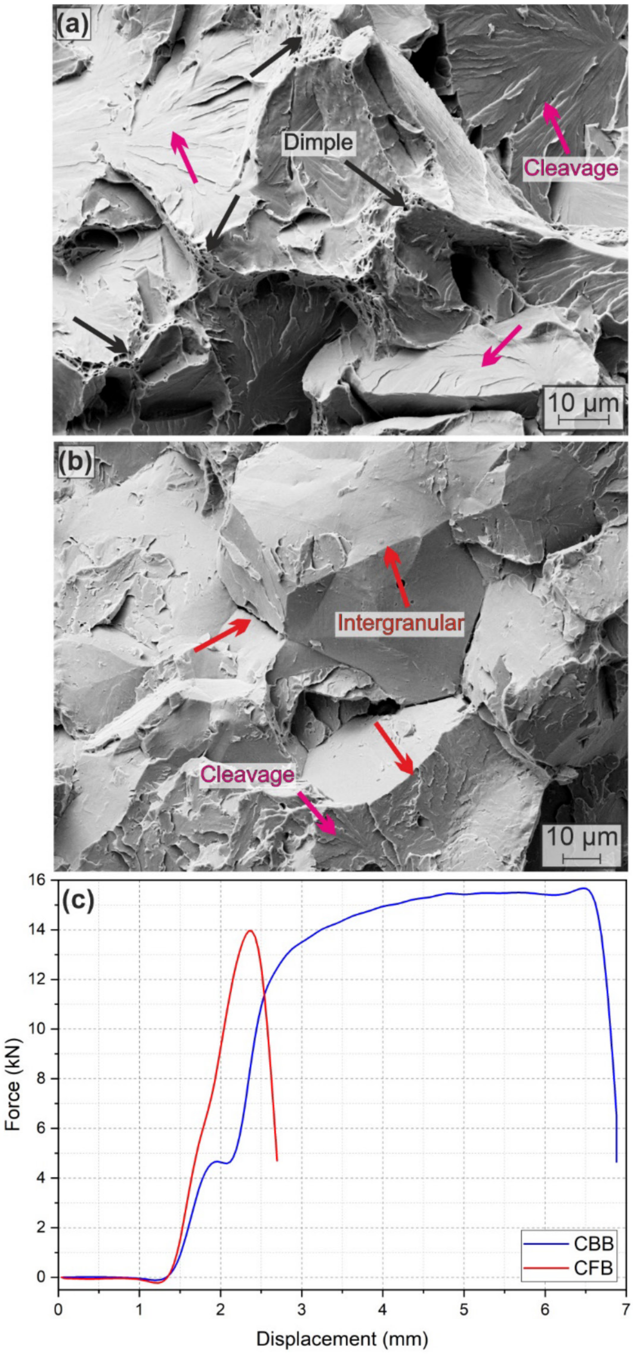

FIGURE 5 | Fracture surface images of (a) CBB and (b) CFB acquired from Charpy impact test specimens. (c) Force-displacement curves of the studied alloys from the Charpy impact test. [Colour figure can be viewed at wileyonlinelibrary.com]

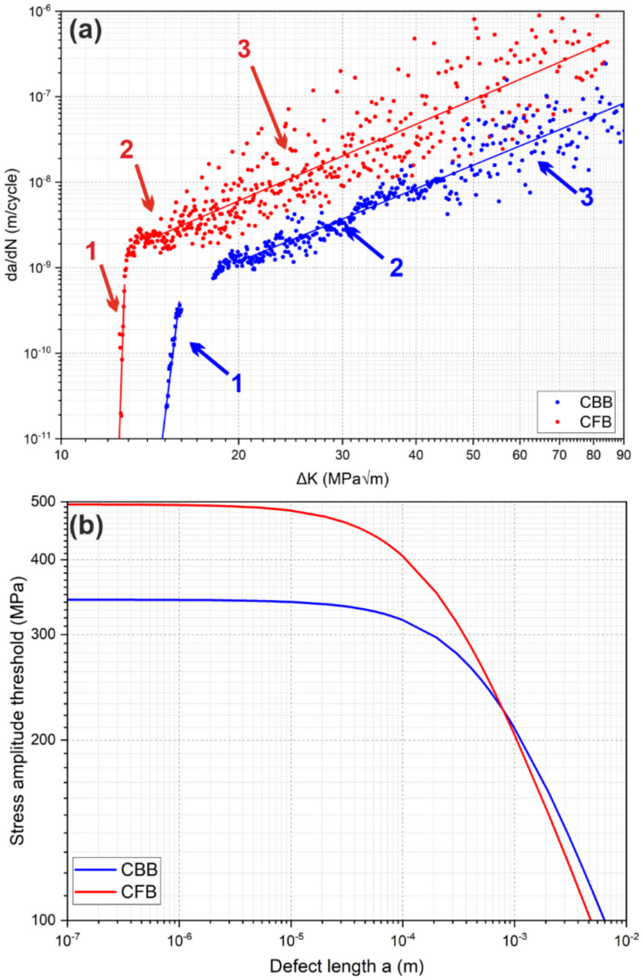

FIGURE 6 | (a) Crack propagation curves and (b) Kitagawa–Takahashi diagram within 10^7 cycles (with El-Haddad modification) of CBB and CFB alloys. Crack propagation curves are divided into three phases to explain the fracture surfaces obtained from the specimens. [Colour figure can be viewed at wileyonlinelibrary.com]

In addition to that, Figure 8b shows the crack deflection possibly on cementite particles, whereas it is also possible that crack deflection might have occurred on a packet/block boundary. However, in the case of CFB, the PAGBs were not effective in deflecting or decelerating the fatigue crack; instead, intergranular and transgranular cracking were observed as in Charpy impact specimens. In Figure 8d, the PAGBs are highlighted along with the MA islands and RA constituents on the boundaries. It can be seen that the propagating crack (in the PAG) coincides with an MA island on a PAGB (Point 1) and continues propagating, causing intergranular fracture until it changes its path (Point 2). Nevertheless, this does not mean that every interaction between the crack and the MA islands causes intergranular fracture during crack propagation tests. As displayed in Figure 8d, the crack leaves the PAGB and enters the adjacent PAG through an MA island (Point 2) with no deflection, causing transgranular fracture. This is shown more clearly in Figure 8e where multiple PAGBs were surpassed with no interference. The IPF map of FCB in Figure 8f supports these findings as well by showing no deflection at the PAGB. Rivetingly, when a PAGB is surpassed transgranularly, instead of a brittle cleavage fracture as in Charpy impact tests, a ductile fracture mechanism was induced.

To explore the crack-PAGB interaction in CFB, the angles between crack paths and PAGBs were further examined. As shown in Figure 8d, the crack propagated along an intergranular path when the angle between the crack and PAGB was relatively large. In contrast, in Figure 8e, the crack cut through the PAGB and propagated on a transgranular path at a smaller angle. Based on these observations, a semiquantitative analysis was conducted to better understand the influence of crack-PAGB geometry on the cracking mechanism in CFB. To this end, the angle between

14602695, 0, Downloaded from https://onlinelibrary.wiley.com/doi/10.1111/ffe.70025 by Rwth Aachen University Zentraler Rechnungseingang, Wiley Online Library on [29/07/2025]. See the Terms and Conditions (https://onlinelibrary.wiley.com/terms-and-conditions) on Wiley Online Library for rules of use; OA articles are governed by the applicable Creative Commons License

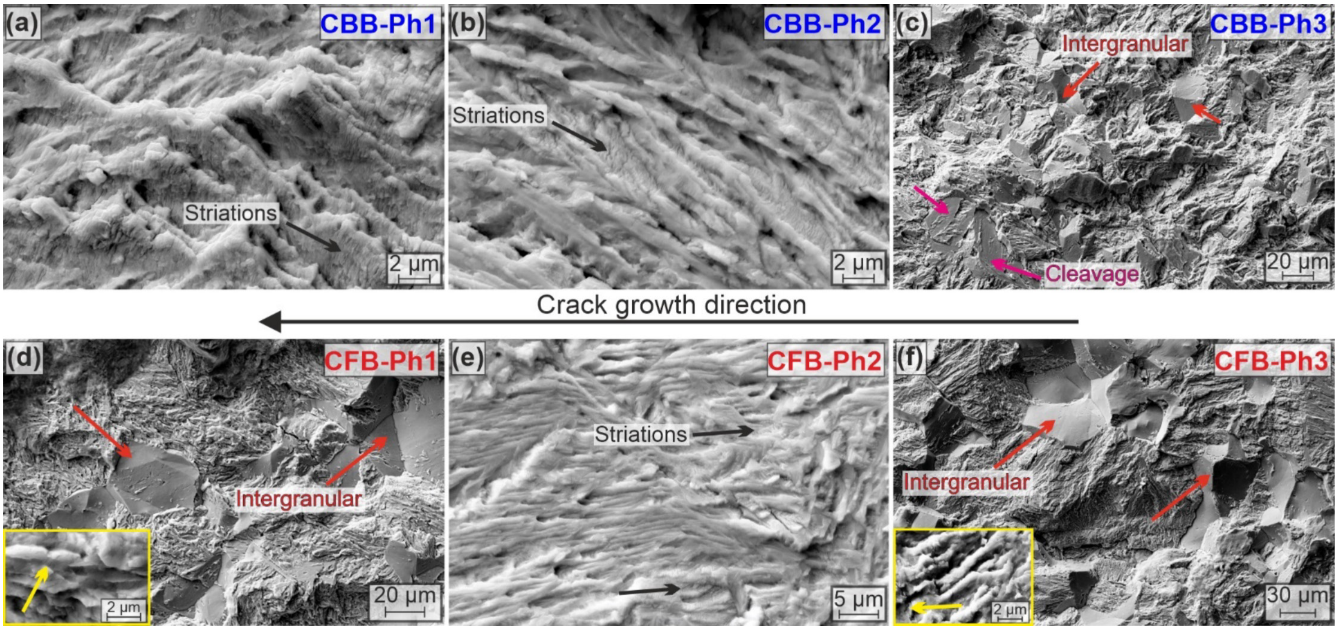

FIGURE 7 | Fracture surface images of (a–c) CBB and (d–f) CFB acquired from crack propagation test specimens. The numbers indicate phases in crack propagation curves. [Colour figure can be viewed at wileyonlinelibrary.com]

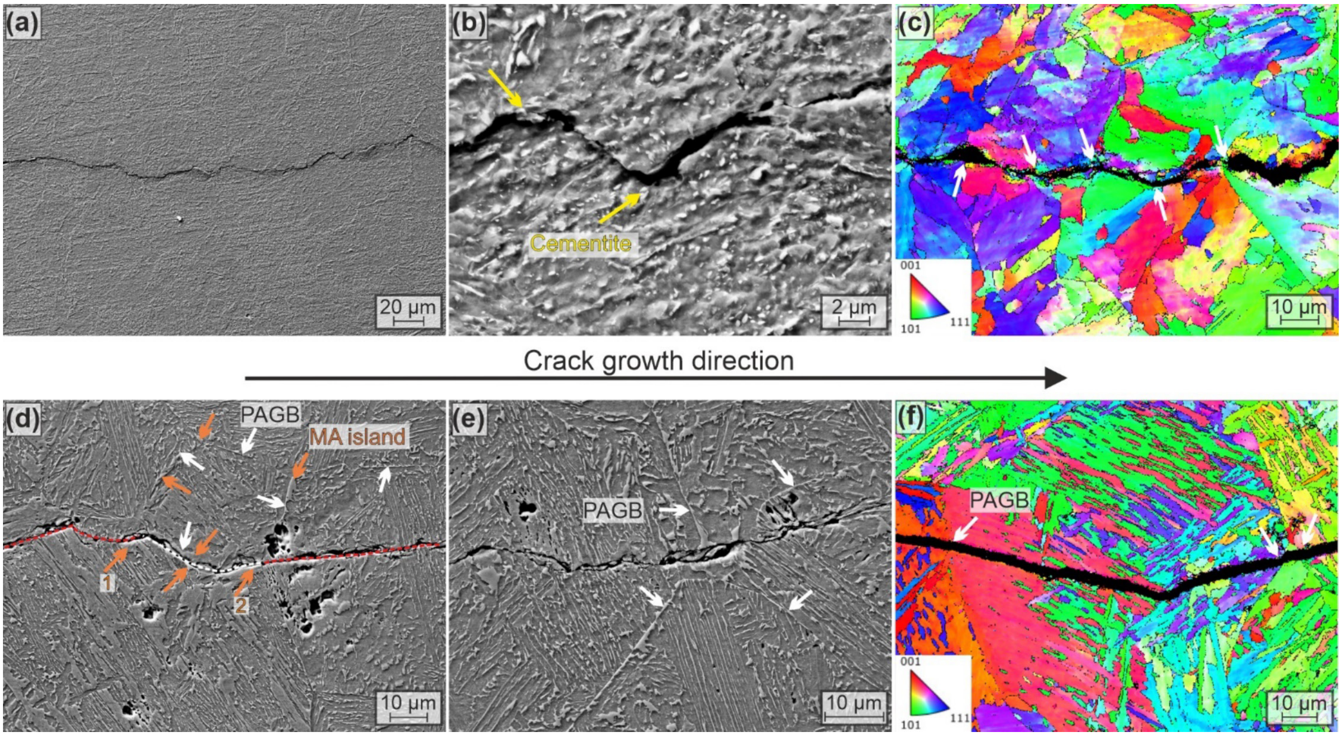

FIGURE 8 | SEM images and inverse pole figure (IPF) maps of (a–c) CBB and (d–f) CFB alloys acquired from the cracked surface perpendicular to the fracture surface. The images were taken from the stable crack growth region. [Colour figure can be viewed at wileyonlinelibrary.com]

the crack and PAGBs was measured at multiple crack-boundary interaction sites. Figure 9 presents the statistical distribution of the measured angles, categorized by crack path. The average angle for intergranular crack propagation was relatively higher, averaging 132°, whereas transgranular cracks occurred at a lower angle of 103°. To provide a standardized interpretation of these results, it can be summarized that intergranular cracks predominantly formed when the angle between the propagating crack and PAGB was above 120°, whereas transgranular cracks were more frequently observed at angles below this threshold.

4 | Discussion

The comparison of the investigated bainitic alloys showed that the deformation behavior of the bainitic steels significantly

14602695, 0, Downloaded from https://onlinelibrary.wiley.com/doi/10.1111/ffe.70025 by Rwth Aachen University Zentraler Rechnungseingang, Wiley Online Library on [29/07/2025]. See the Terms and Conditions (https://onlinelibrary.wiley.com/terms-and-conditions) on Wiley Online Library for rules of use; OA articles are governed by the applicable Creative Commons License

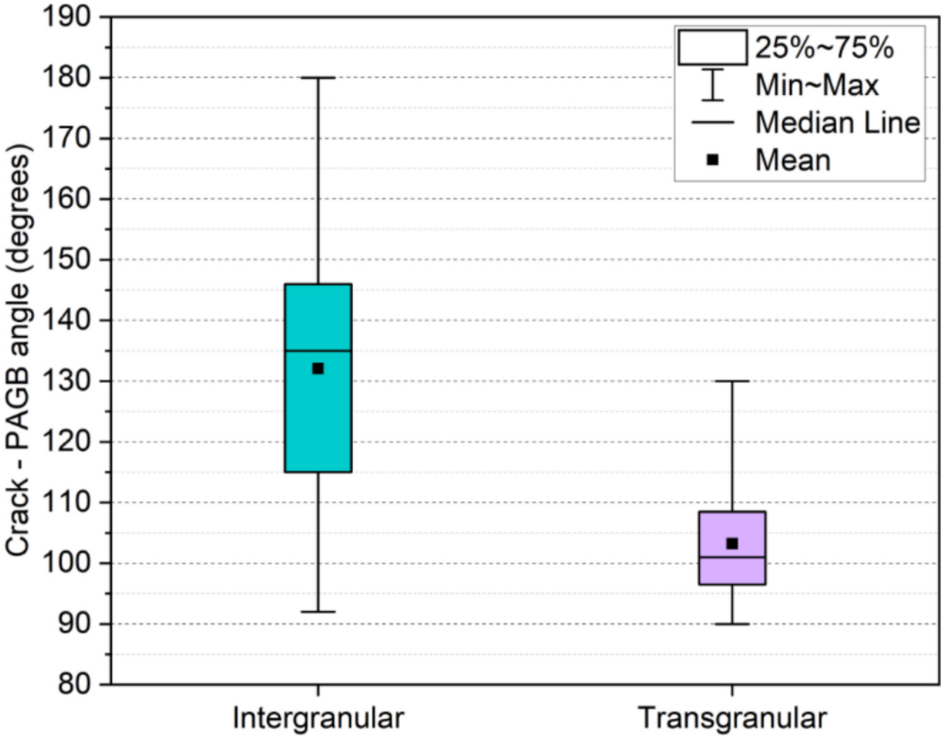

FIGURE 9 | Statistical distribution of the angles between the propagating crack and PAGBs for intergranular and transgranular crack paths in CFB. The plot shows the minimum and maximum values, mean, median, and interquartile range (25th–75th percentile). [Colour figure can be viewed at wileyonlinelibrary.com]

depends on the deformation mechanism, which in turn is controlled by the microstructural constituents. Many studies have shown that the existence of RA as the secondary phase instead of cementite improves the quasistatic tensile properties of bainitic steels [9, 10], which was confirmed by our investigations (cf. Figure 3a and Table 3). The lattice resistance of the face-centered cubic (FCC) RA phase is lower than that of the body-centered cubic (BCC) BF phase, which can additionally facilitate more dislocation motion. Hence, plasticity is improved [11]. Contrariwise, the CFB alloy achieved very low impact toughness values, showing a combination of transgranular and intergranular fracture (cf. Figures 4c,d and 5b), whereas the CBB alloy reached substantially higher impact toughness values with a considerable amount of ductile areas in the fracture surface (cf. Figures 4a,b and 5a). It was shown in multiple studies that the MA islands, which formed on PAGBs, could result in a loss of impact toughness [14, 22–26]. When austenite transforms to martensite during cooling (forming MA islands), a certain volume expansion occurs due to the nature of this transformation. As a result of this, the stress concentration in the surrounding bainitic matrix can increase, assisting the cleavage fracture [22]. In addition to that, the hardness of the MA islands is significantly higher than the surrounding bainite, causing a stress concentration in the adjacent matrix. During loading, a large stress could be generated at the interface of MA islands and matrix, which results in the debonding of MA constituents from PAGB boundaries, leading to cleavage fracture. Moreover, the MA islands are naturally brittle, and this increases the stress concentration at the PAGB. As a result, PAGBs may weaken and act as initiation sites for cracks and/or promote crack propagation [25]. Another reason behind the change in the fracture mode could be the change in the transformation rate of RA to martensite in different tests. In uniaxial tensile tests, due to lower strain rate and uniform deformation, the RA austenite gradually transforms to martensite, leading to enhanced elongation and high UTS values [27]. With an increased strain rate, localized deformation, and multiaxial stress state in the Charpy impact test, the RA transforms to martensite faster at the crack tip. The MA islands and RA along the PAGB boundaries continuously transform to martensite at the crack tip, forming a brittle network. This could cause a path for brittle crack propagation through PAGB, leading to intergranular debonding [27]. On the other hand, CBB exhibited a significant amount of ductile regions with no indication of intergranular fracture. Therefore, it can be concluded that cementite precipitation did not compromise PAGBs, which may have led to additional brittleness as in CFB. Furthermore, cementite particles may have prevented the continuous crack paths by deflecting the crack. In literature, it was also mentioned that cementite particles may promote microvoid formation and coalescence, leading to ductile fracture modes [28].

The fatigue limit of CFB is significantly higher than that of CBB (cf. Table 3), which is in good agreement with the quasistatic tensile properties, confirming the well-known relationship between the UTS of metallic materials and their fatigue limit [29, 30]. The fatigue limit of the materials is more related to the crack initiation phase, which can take a long time, especially under high-cycle fatigue regimes. To generate this, the fatigue tests to determine the fatigue limit were conducted in the absence of a notch, in a polished “crack-free” condition. The materials with higher UTS require higher stresses to nucleate and grow persistent slip bands to form a crack. Therefore, the higher

14602695, 0, Downloaded from https://onlinelibrary.wiley.com/doi/10.1111/ffe.70025 by Rwth Aachen University Zentraler Rechnungseingang, Wiley Online Library on [29/07/2025]. See the Terms and Conditions (https://onlinelibrary.wiley.com/terms-and-conditions) on Wiley Online Library for rules of use; OA articles are governed by the applicable Creative Commons License

fatigue limit of CFB can be attributed to its significantly higher UTS compared to CBB.

On the other hand, based on previous investigations [12] and literature data [11, 31], it can be said that unexpected results were obtained from crack propagation tests of CFB by exhibiting poorer crack propagation characteristics than CBB (cf. Table 3). In normal circumstances, PAG and block boundaries are effective microstructural barriers to deflect the propagating fatigue crack due to their highly misoriented nature [32]. The crack path of CBB alloy revealed that the existence of brittle cementite did not compromise the effect of high-angle boundaries during crack propagation. As presented in Figure 8, the crack was effectively deflected at these boundaries, indicating that the fatigue crack growth is mainly controlled by PAG, packet, and block boundaries in CBB. Additionally, it was mentioned that cementite plates can be strong barriers to fatigue cracks under cyclic loading and slow down fatigue crack growth [33, 34]. The fracture surfaces in Figure 7a–c strengthen this statement by showing ductile characteristics with fatigue striations. Moreover, the SEM images acquired perpendicular to the fracture surface reveal the small deflections at cementite precipitates, as shown in Figure 8b.

On the other hand, these boundaries, particularly PAGBs, were not effective in the case of CFB and either caused an intergranular fracture or a transgranular cracking of PAGB without deflection (cf. Figure 8d–f). Gao et al. [13] stated that MA islands and blocky RA, which are located at the PAGBs, may induce intergranular fatigue cracking due to the slip impingement effect. The RA phase (FCC) has more slip systems compared to the BF phase (BCC). It was accordingly stated that on the slip impingement, where MA islands and/or unstable blocky RA exist in adjacent PAGs, the activation of the preferred slip plane becomes easier, leading to intergranular fatigue cracking [13]. As the threshold SIF range, ΔK_{th}, is primarily associated with the crack propagation resistance of the microstructure against existing cracks. Accordingly, to determine ΔK_{th}, the bending fatigue experiments were performed using SENB specimens with precracks deliberately introduced at the notch roots. The higher ΔK_{th} of CBB can be attributed to pure ductile fracturing behavior in phases 1 (cf. Figure 7a). However, CFB has more brittle behavior during Phase 1 with intergranular fracture due to the existence of MA islands and low-stable austenitic constituents on PAGBs (cf. Figure 7d), leading to deterioration of ΔK_{th}.

Furthermore, in the event of transgranular cracking through PAGBs with no deflection, a ductile fracture mechanism was induced, unlike in Charpy impact tests. This suggests that the deformation rate was not sufficient to debond the whole grain during crack propagation tests, although the PAGBs became brittle enough to be surpassed due to MA islands and low-stable austenitic constituents. Therefore, a ductile fracture was observed when the fatigue crack passed through the PAGBs. In addition to that, when the crack propagation curves are compared, there is more data scattering observed in the stable crack growth region of CFB (cf. Figure 6a). In the case of CBB, at higher ΔK values, the data started to scatter as well (Phase 3 of the stable crack propagation region, highlighted in Figure 6a). In this region, some cleavage and intergranular fractures also occurred in CBB (cf. Figure 7c). Therefore, the reason behind the data scattering could be the manifestation of both brittle and ductile fractures during the loading.

The results show that the PAGBs in CFB are weakened in the vicinity of the MA islands, and low-stable austenitic constituents, leading to brittleness and reducing the effectiveness of these boundaries against propagating cracks (cf. Figure 8a–c). Besides, it is also crucial to understand the mechanism governing the crack path during loading, especially for improved microstructure optimization. The analysis suggests that the angle between the propagating crack and PAGBs influences the crack path in the CFB microstructure (cf. Figure 9), with intergranular cracks forming at angles of 120° or greater, whereas transgranular cracks occurred primarily at angles below 120°. This possible scenario is illustrated in Figure 10, which shows the tendency of cracks to follow an intergranular path along PAGBs through a brittle necklace formed by MA islands and austenitic constituents with a large crack-boundary angle encounter.

In the literature, metastable RA is mostly known to improve fatigue properties of high-strength steels by transforming to martensite due to the TRIP effect caused by the plastic deformation at the crack tip [11, 35–38]. Due to the phase transformation and formation of compressive stresses, the energy of the crack is absorbed, and thus, the crack can be decelerated or deflected. However, the current study shows that this is not straightforward for RA-containing bainitic microstructures. Based on the results, it can be concluded that the reason for obtaining poor crack propagation characteristics in CFB alloy, despite the higher UTS and fatigue limit, is probably due to the weakened nature of PAGBs, easing the fatigue crack to propagate. This points out the detrimental nature of the MA island and unstable RA phases on PAGBs. In the meantime, observing ductile regions confirms the plasticity during deformation and the beneficial features of BF plates and RA films in the CFB microstructure. It is well known that film-like RA is mechanically more stable compared to blocky RA and MA islands [5]. This means that in the case of plastic deformation and, consequently, the occurrence of martensitic transformation in front of a crack tip, parallelly aligned RA films between BF plates in PAGs will

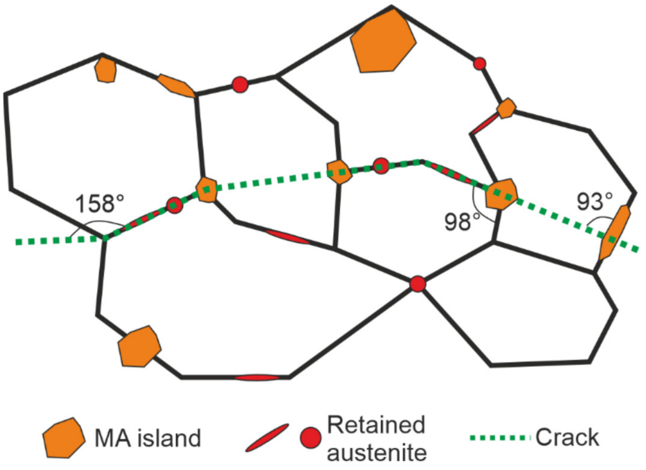

FIGURE 10 | Schematic illustration of the fracture mechanism in CFB alloy. [Colour figure can be viewed at wileyonlinelibrary.com]

14602695, 0, Downloaded from https://onlinelibrary.wiley.com/doi/10.1111/ffe.70025 by Rwth Aachen University Zentraler Rechnungseingang, Wiley Online Library on [29/07/2025]. See the Terms and Conditions (https://onlinelibrary.wiley.com/terms-and-conditions) on Wiley Online Library for rules of use; OA articles are governed by the applicable Creative Commons License

consume more energy than significantly metastable MA islands or austenitic constituents on PAGBs. This points out that with microstructure optimization through adjustments in chemical composition and processing, the formation, size, and fraction of MA islands and unstable austenitic constituents (especially on PAGBs) can be reduced, the stability of austenite can be optimized, and the brittle behavior during crack propagation can be minimized.

5 | Conclusion

The deformation behavior of carbide-bearing (CBB) and carbide-free bainite (CFB) was investigated under different loading conditions. To achieve this, uniaxial tensile, fatigue crack propagation, and instrumented Charpy impact tests, along with thorough microstructural and fractographic investigations, were employed. The following conclusions can be drawn.

1. The optimization of microstructure, especially retained austenite (RA), in CFB is critical to achieve optimum mechanical performance under varying loading conditions. The formation of martensite-austenite (MA) islands and unstable austenitic constituents at prior austenite grain boundaries (PAGB) has a detrimental effect on fracture behavior when deformation progression is localized, as in Charpy impact and fatigue crack propagation tests.
2. CFB outperforms CBB in quasistatic tensile properties mainly due to the gradual transformation of RA to martensite, which improves ductility and strength during uniformly distributed deformation at lower strain rates.
3. CBB shows significantly higher impact toughness, with notable ductile regions in the fracture surface, whereas CFB exhibits brittle behavior. The existence of brittle MA islands and sudden transformation of RA at higher strain rates, combined with a localized deformation mechanism, promotes a brittle network along the PAGBs, causing intergranular fracture or rapid debonding of PAGs through MA islands, causing cleavage fracture.
4. Despite the higher fatigue limit, CFB shows a higher fatigue crack propagation rate and lower threshold of stress intensity factor range ΔK_{th} than CBB. Although PAGBs in CBB successfully deflect the fatigue cracks, MA islands and unstable austenitic constituents in CFB weaken these boundaries, resulting in intergranular fractures through the brittle network or cracks that cut PAGBs without deflection. However, ductile fracture behavior is observed when the crack goes through a PAG instead of cleavage fracture, highlighting the influence of a lower deformation rate compared to Charpy impact tests.

In summary, the comparison of the investigated bainitic steel concepts reveals that the most desirable microstructure for bainite is not trivial to define. Although the majority of the studies refer to the benefits of austenite-containing bainitic steels, the drawbacks concerning Charpy impact toughness and fatigue crack propagation characteristics need to be considered in dependence on the intended application.

Acknowledgments

The authors would like to thank Dr. Marion Kreins for the fruitful discussions. Open Access funding enabled and organized by Projekt DEAL.

Conflicts of Interest

The authors declare no conflicts of interest.

Data Availability Statement

The data that support the findings of this study are available from the corresponding author upon reasonable request.

References

1. A. Gramlich, W. Hagedorn, K. Greiff, and U. Krupp, “Air Cooling Martensites—The Future of Carbon Neutral Steel Forgings?,” *Advanced Engineering Materials* 25 (2023): 2201931.

2. W. Hagedorn, A. Gramlich, K. Greiff, and U. Krupp, “Alloy and Process Design of Forging Steels for Better Environmental Performance,” *Sustainable Materials and Technologies* 34 (2022): e00509.

3. C. Hofer, F. Winkelhofer, H. Clemens, and S. Primig, “Morphology Change of Retained Austenite During Austempering of Carbide-Free Bainitic Steel,” *Materials Science and Engineering A* 664 (2016): 236–246.

4. K. Wang, Z. Tan, G. Gao, et al., “Microstructure-Property Relationship in Bainitic Steel: The Effect of Austempering,” *Materials Science and Engineering A* 675 (2016): 120–127.

5. H. K. D. H. Bhadeshia and D. V. Edmonds, “Bainite in Silicon Steels: New Composition–Property Approach Part 1,” *Metal Science* 17 (1983): 411–419.

6. F. G. Caballero, H. Roelofs, S. Hasler, et al., “Influence of Bainite Morphology on Impact Toughness of Continuously Cooled Cementite Free Bainitic Steels,” *Materials Science and Technology* 28 (2012): 95–102.

7. E. Kozeschnik and H. K. D. H. Bhadeshia, “Influence of Silicon on Cementite Precipitation in Steels,” *Materials Science and Technology* 24 (2008): 343–347.

8. F. G. Caballero, C. GarcíA-Mateo, J. Chao, M. J. Santofimia, C. Capdevila, and C. G. de Andrés, “Effects of Morphology and Stability of Retained Austenite on the Ductility of TRIP-Aided Bainitic Steels,” *ISIJ International* 48 (2008): 1256–1262.

9. C. Hofer, S. Primig, H. Clemens, F. Winkelhofer, and R. Schnitzer, “Influence of Heat Treatment on Microstructure Stability and Mechanical Properties of a Carbide-Free Bainitic Steel,” *Advanced Engineering Materials* 19 (2017): 1600658.

10. C. Garcia-Mateo and F. G. Caballero, “The Role of Retained Austenite on Tensile Properties of Steels With Bainitic Microstructures,” *Materials Transactions* 46 (2005): 1839–1846.

11. X. Long, F. Zhang, Z. Yang, and B. Lv, “Study on Microstructures and Properties of Carbide-Free and Carbide-Bearing Bainitic Steels,” *Materials Science and Engineering A* 715 (2018): 10–16.

12. O. Gulbay, M. Ackermann, A. Gramlich, A. R. Durmaz, I. Steinbach, and U. Krupp, “Influence of Transformation Temperature on the High-Cycle Fatigue Performance of Carbide-Bearing and Carbide-Free Bainite,” *Steel Research International* 94 (2023): 2300238.

13. G. Gao, R. Liu, K. Wang, X. Gui, R. Misra, and B. Bai, “Role of Retained Austenite With Different Morphologies on Sub-Surface Fatigue Crack Initiation in Advanced Bainitic Steels,” *Scripta Materialia* 184 (2020): 12–18.

14. F. Zhao, L. Morales-Rivas, Q. Yu, G. Wang, F. G. Caballero, and D. San-Martin, “Unforeseen Influence of the Prior Austenite Grain Size on

14602695, 0, Downloaded from https://onlinelibrary.wiley.com/doi/10.1111/ffe.70025 by Rwth Aachen University Zentraler Rechnungseingang, Wiley Online Library on [29/07/2025]. See the Terms and Conditions (https://onlinelibrary.wiley.com/terms-and-conditions) on Wiley Online Library for rules of use; OA articles are governed by the applicable Creative Commons License

the Mechanical Properties of a Carbide-Free Bainitic Steel," *Materials Science and Engineering A* 881 (2023): 145388.

15. N. Huda, A. R. H. Midawi, J. Gianetto, R. Lazor, and A. P. Gerlich, "Influence of Martensite-Austenite (MA) on Impact Toughness of X80 Line Pipe Steels," *Materials Science and Engineering A* 662 (2016): 481–491.

16. C. Xie, Z. Liu, X. He, X. Wang, and S. Qiao, "Effect of Martensite–Austenite Constituents on Impact Toughness of Pre-Tempered MnNiMo Bainitic Steel," *Materials Characterization* 161 (2020): 110139.

17. O. Gulbay, A. Gramlich, and U. Krupp, "Effects of Silicon and Aluminum Alloying on Phase Transformation and Microstructure Evolution in Fe–0.2C–2.5Mn Steel: Insights From Continuous–Cooling–Transformation and Time–Temperature–Transformation Diagrams," *Steel Research International* 95 (2024): 2400159.

18. International Organization for Standardization, *Metallic Materials: Fatigue Testing: Fatigue Crack Growth Method*. ISO 12108, (ISO, 2002).

19. W. J. Dixon and A. M. Mood, "A Method for Obtaining and Analyzing Sensitivity Data," *Journal of the American Statistical Association* 43 (1948): 109–126.

20. H. Kitagawa and S. Takahashi, "Applicability of Fracture Mechanics to Very Small Cracks or the Cracks in the Early Stage," in *Proceedings of the 2nd International Conference on Mechanical Behaviour of Materials* (1976): 627–631. American Society for Metals (now ASM International).

21. M. H. el Haddad, T. H. Topper, and K. N. Smith, "Prediction of Non Propagating Cracks," *Engineering Fracture Mechanics* 11 (1979): 573–584.

22. P. Mohseni, J. K. Solberg, M. Karlsen, O. M. Akselsen, and E. Østby, "Investigation of Mechanism of Cleavage Fracture Initiation in Intercritically Coarse Grained Heat Affected Zone of HSLA Steel," *Materials Science and Technology* 28 (2012): 1261–1268.

23. P. Mohseni, J. K. Solberg, M. Karlsen, O. M. Akselsen, and E. Østby, "Cleavage Fracture Initiation at M–A Constituents in Intercritically Coarse-Grained Heat-Affected Zone of a HSLA Steel," *Metallurgical and Materials Transactions A* 45 (2014): 384–394.

24. Y. Li and T. N. Baker, "Effect of Morphology of Martensite–Austenite Phase on Fracture of Weld Heat Affected Zone in Vanadium and Niobium Microalloyed Steels," *Materials Science and Technology* 26 (2010): 1029–1040.

25. A. Lambert-Perlade, A. F. Gourgues, J. Besson, T. Sturel, and A. Pineau, "Mechanisms and Modeling of Cleavage Fracture in Simulated Heat-Affected Zone Microstructures of a High-Strength Low Alloy Steel," *Metallurgical and Materials Transactions A* 35 (2004): 1039–1053.

26. Z. Li, L. Tian, B. Jia, and S. Li, "A New Method to Study the Effect of M–A Constituent on Impact Toughness of IC HAZ in Q690 Steel," *Journal of Materials Research* 30 (2015): 1973–1978.

27. Z. Xiong, P. J. Jacques, A. Perlade, and T. Pardoen, "Ductile and Intergranular Brittle Fracture in a Two-Step Quenching and Partitioning Steel," *Scripta Materialia* 157 (2018): 6–9.

28. T. Tokunaga, K. Yamamoto, Y. Minamino, T. Takayama, T. Sugimoto, and K. Hagihara, "Effects of Cementite Particles on Impact Properties in High-Hardness Hypereutectoid Steels," *ISIJ International* 64 (2024): 389–400.

29. J. C. Pang, S. X. Li, Z. G. Wang, and Z. F. Zhang, "General Relation Between Tensile Strength and Fatigue Strength of Metallic Materials," *Materials Science and Engineering A* 564 (2013): 331–341.

30. J. C. Pang, S. X. Li, Z. G. Wang, and Z. F. Zhang, "Relations Between Fatigue Strength and Other Mechanical Properties of Metallic Materials," *Fatigue & Fracture of Engineering Materials & Structures* 37 (2014): 958–976.

31. R. Branco, F. Berto, F. Zhang, X. Long, and J. D. Costa, "Comparative Study of the Uniaxial Cyclic Behaviour of Carbide-Bearing and Carbide-Free Bainitic Steels," *Metals* 8 (2018): 422.

32. X. Y. Qi, L. X. Du, J. Hu, and R. Misra, "High-Cycle Fatigue Behavior of Low-C Medium-Mn High Strength Steel With Austenite-Martensite Submicron-Sized Lath-Like Structure," *Materials Science and Engineering A* 718 (2018): 477–482.

33. K. Hussain, "Short Fatigue Crack Behaviour and Analytical Models: A Review," *Engineering Fracture Mechanics* 58 (1997): 327–354.

34. U. Krupp, *Fatigue Crack Propagation in Metals and Alloys: Microstructural Aspects and Modelling Concepts* (Chichester, Weinheim: John Wiley distributor; Wiley-VCH, 2007).

35. C. Y. Huo and H. L. Gao, "Strain-Induced Martensitic Transformation in Fatigue Crack Tip Zone for a High Strength Steel," *Materials Characterization* 55 (2005): 12–18.

36. T. B. Hilditch, I. B. Timokhina, L. T. Robertson, E. V. Pereloma, and P. D. Hodgson, "Cyclic Deformation of Advanced High-Strength Steels: Mechanical Behavior and Microstructural Analysis," *Metallurgical and Materials Transactions A* 40 (2009): 342–353.

37. M. Abareshi and E. Emadoddin, "Effect of Retained Austenite Characteristics on Fatigue Behavior and Tensile Properties of Transformation Induced Plasticity Steel," *Materials & Design* 32 (2011): 5099–5105.

38. I. de Diego-Calderón, P. Rodriguez-Calvillo, A. Lara, et al., "Effect of Microstructure on Fatigue Behavior of Advanced High Strength Steels Produced by Quenching and Partitioning and the Role of Retained Austenite," *Materials Science and Engineering A* 641 (2015): 215–224.

14602695, 0, Downloaded from https://onlinelibrary.wiley.com/doi/10.1111/ffe.70025 by Rwth Aachen University Zentraler Rechnungseingang, Wiley Online Library on [29/07/2025]. See the Terms and Conditions (https://onlinelibrary.wiley.com/terms-and-conditions) on Wiley Online Library for rules of use; OA articles are governed by the applicable Creative Commons License